AFRL-RZ-WP-TP-2007-249

USE OF MEASURED SPECIES CLASS CONCENTRATIONS WITH CHEMICAL KINETIC MODELING FOR THE PREDICTION OF AUTOXIDATION AND DEPOSITION OF JET FUELS (POSTPRINT)

Nicholas J. Kuprowicz, Steven Zabarnick, Zachary J. West, and Jamie S. Ervin

Fuels Branch
Turbine Engine Division

FEBRUARY 2007

AIR FORCE RESEARCH LABORATORY
PROPULSION DIRECTORATE
WRIGHT-PATTERSON AIR FORCE BASE, OH 45433-7251
AIR FORCE MATERIEL COMMAND
UNITED STATES AIR FORCE

REPORT DOCUMENTATION PAGE

Form Approved
OMB No. 0704-0188

1. REPORT DATE *(DD-MM-YY)*	2. REPORT TYPE	3. DATES COVERED *(From - To)*
February 2007	Journal Article Postprint	01 January 2005 – 01 February 2007

4. TITLE AND SUBTITLE
USE OF MEASURED SPECIES CLASS CONCENTRATIONS WITH CHEMICAL KINETIC MODELING FOR THE PREDICTION OF AUTOXIDATION AND DEPOSITION OF JET FUELS (POSTPRINT)

5a. CONTRACT NUMBER
In-house

5b. GRANT NUMBER

5c. PROGRAM ELEMENT NUMBER
62203F

6. AUTHOR(S)
Nicholas J. Kuprowicz (AFRL/RZTA) and Steven Zabarnick (AFRL/RZTG)
Zachary J. West and Jamie S. Ervin (University of Dayton)

5d. PROJECT NUMBER
3048

5e. TASK NUMBER
05

5f. WORK UNIT NUMBER
304805F1

7. PERFORMING ORGANIZATION NAME(S) AND ADDRESS(ES)

Engine Integration and Assessment Branch (AFRL/RZTA)
and Fuels Branch (AFRL/RZTG), Turbine Engine Division
Air Force Research Laboratory, Propulsion Directorate
Wright-Patterson Air Force Base, OH 45433-7251
Air Force Materiel Command, United States Air Force

University of Dayton
Dayton, OH 45469-0232

8. PERFORMING ORGANIZATION REPORT NUMBER
AFRL-RZ-WP-TP-2007-249

9. SPONSORING/MONITORING AGENCY NAME(S) AND ADDRESS(ES)
Air Force Research Laboratory
Propulsion Directorate
Wright-Patterson Air Force Base, OH 45433-7251
Air Force Materiel Command
United States Air Force

10. SPONSORING/MONITORING AGENCY ACRONYM(S)
AFRL/RZTG

11. SPONSORING/MONITORING AGENCY REPORT NUMBER(S)
AFRL-RZ-WP-TP-2007-249

12. DISTRIBUTION/AVAILABILITY STATEMENT
Approved for public release; distribution unlimited.

13. SUPPLEMENTARY NOTES
Journal article published in Energy & Fuels, 2007, Vol. 21.

PAO Case Number: AFRL/WS 06-2204, 14 Sep 2006.

14. ABSTRACT
The production of detrimental carbonaceous deposits in jet aircraft fuel systems results from the involvement of trace heteroatomic species in the autoxidation chain that occurs upon fuel heating. Although it has been known for many years that these sulfur-, nitrogen-, and oxygen-containing species contribute to the tendency of a fuel to form deposits, simple correlations have been unable to predict the oxidation rates or the deposit forming tendencies over a range of fuel samples. In the present work, a chemical kinetic mechanism developed previously is refined to include the roles of key fuel species classes, such as phenols, reactive sulfur species, dissolved metals, and hydroperoxides. The concentrations of these fuel species classes in the unreacted fuel samples are measured experimentally and used as an input to the mechanism. The resulting model is used to simulate autoxidation behavior observed over a range of fuel samples.

15. SUBJECT TERMS
jet fuel, thermal stability, autoxidation, deposits, heteroatoms, kinetic mechanism

16. SECURITY CLASSIFICATION OF:			17. LIMITATION OF ABSTRACT:	18. NUMBER OF PAGES	19a. NAME OF RESPONSIBLE PERSON (Monitor)
a. REPORT	b. ABSTRACT	c. THIS PAGE			Tim Edwards
Unclassified	Unclassified	Unclassified	SAR	22	19b. TELEPHONE NUMBER *(Include Area Code)* N/A

Standard Form 298 (Rev. 8-98)
Prescribed by ANSI Std. Z39-18

Use of Measured Species Class Concentrations with Chemical Kinetic Modeling for the Prediction of Autoxidation and Deposition of Jet Fuels

Nicholas J. Kuprowicz,[†,§] Steven Zabarnick,*[,‡,§] Zachary J. West,[‡,§] and Jamie S. Ervin[‡,§]

Air Force Research Laboratory, Propulsion Directorate, Wright-Patterson Air Force Base, Ohio 45433, Energy & Environmental Engineering Division, University of Dayton Research Institute, Dayton, Ohio 45469-0116, and Department of Mechanical & Aerospace Engineering, University of Dayton, Dayton, Ohio 45469-0232

Received August 17, 2006. Revised Manuscript Received November 27, 2006

The production of detrimental carbonaceous deposits in jet aircraft fuel systems results from the involvement of trace heteroatomic species in the autoxidation chain that occurs upon fuel heating. Although it has been known for many years that these sulfur-, nitrogen-, and oxygen-containing species contribute to the tendency of a fuel to form deposits, simple correlations have been unable to predict the oxidation rates or the deposit forming tendencies over a range of fuel samples. In the present work, a chemical kinetic mechanism developed previously is refined to include the roles of key fuel species classes, such as phenols, reactive sulfur species, dissolved metals, and hydroperoxides. The concentrations of these fuel species classes in the unreacted fuel samples are measured experimentally and used as an input to the mechanism. The resulting model is used to simulate autoxidation behavior observed over a range of fuel samples. The model includes simulation of the consumption of dissolved oxygen, as well as the formation and consumption of hydroperoxide species during thermal exposure. In addition, the chemical kinetic mechanism is employed with a global deposition submechanism in computational fluid dynamics (CFD) simulations of deposit formation occurring in near-isothermal as well as non-isothermal flowing environments. Experimental measurements of oxygen consumption, hydroperoxide formation, and deposition are performed for a set of seven fuels. Comparison with experimental measurements indicates that the methodology offers the ability to predict both oxidation and deposition rates in complex flow environments, such as aircraft fuel systems, using only measured chemical species class concentrations for the fuel of interest.

Introduction

Prior to being combusted for propulsion, jet fuel is heated during passage through aircraft fuel system components. This heating occurs incidentally while passing through fuel pumps but is promoted via heat exchangers, particularly in advanced military aircraft, to remove excess heat from numerous aircraft subsystems. Systems which may require cooling include avionics, hydraulics, lubrication, and environmental control. The use of fuel to cool fuel system, engine, and airframe components is an enabling technology for advanced military aircraft due to the large quantity of excess heat produced. Unfortunately, the heat absorbed by the fuel is not always innocuous. When fuel temperatures approach ∼140 °C, the fuel begins to react via an autoxidation chain mechanism with the small amount of dissolved oxygen (65−75 ppmwt)[1] present from exposure to air. These autoxidation reactions ultimately result in the formation of detrimental surface deposits and bulk insolubles.[2] These deposits can plug narrow passageways in valves, filters, and nozzles and can inhibit the desired heat transfer in heat exchangers. Numerous techniques have been investigated to limit the formation of deposits, including the following: fuel system designs to minimize fuel temperatures, fuel additives to inhibit autoxidation and/or deposit formation, fuel deoxygenation, fuel system surface coatings, and inclusion of "sacrificial" or coke tolerant components.[3] But, no single method is able to eliminate the deposition problem under all current and proposed aircraft fuel system conditions.

In recent years, chemical kinetic models have been developed which simulate the major autoxidation pathways that occur in jet fuels.[4−6] The development of a widely applicable autoxidation mechanism, which enables the prediction of deposit formation, would greatly aid the fuel system design process and enable the more efficient use of the fuel as a heat sink.[7] As jet fuels consist of hundreds of individual species, which vary in their identity and concentration in different fuel samples, it is impractical to build detailed chemical kinetic mechanisms. Grouped or lumped mechanisms, sometimes referred to as

* Corresponding author. Tel.: 937-255-3549. E-mail: Steven.Zabarnick@wpafb.af.mil.

† Air Force Research Laboratory.

‡ University of Dayton Research Institute.

§ University of Dayton.

(1) Striebich, R. C.; Rubey, W. A. *Prepr. Pap,—Am. Chem. Soc., Div. Pet. Chem.* **1994**, *39*, 47−50.

(2) Hazlett, R. N. *Thermal Oxidation Stability of Aviation Turbine Fuels*; ASTM: Philadelphia, 1991.

(3) Heneghan, S. P.; Zabarnick, S.; Ballal, D. R.; Harrison, W. E. *J. Energy Res. Tech.* **1996**, *118*, 170−179.

(4) Zabarnick, S. *Ind. Eng. Chem. Res.* **1993**, *32*, 1012−1017.

(5) Zabarnick, S. *Energy Fuels* **1998**, *12*, 547−553.

(6) Kuprowicz, N. J.; Ervin, J. S.; Zabarnick, S. *Fuel.* **2004**, *83*, 1795−1801.

(7) Balster, L. M.; Zabarnick, S.; Ervin, J. S.; Striebich, R.; DeWitt, M. J.; Doungthip, T. Predicting the Thermal Stability of Jet Fuel: Analytical Techniques Toward Model Validation. *Proceedings of the 8th International Conference on Stability, Handling, and Use of Liquid Fuels*, Steamboat Springs, CO, 2004.

10.1021/ef060391o CCC: $37.00
Published on Web 02/01/2007

"pseudo-detailed" mechanisms, have been used to simulate the most important reactive pathways, including the effects of antioxidants and catalytic surfaces.[4−6,8] In addition, these mechanisms have been combined with computational fluid dynamics techniques with the goal of simulating the complex time and temperature variation during fuel flow in aircraft fuel system components.[8,9] Most recently, initial efforts at including global deposit formation reactions in these mechanisms have been performed.[7,10] An initial goal in the development of these models is to allow prediction of oxidation and deposition under simple laboratory flow systems with near-isothermal temperatures, with the ultimate goal of simulation of complex flow systems, such as engine nozzles, which exhibit highly non-isothermal fuel exposure.

The present work details the development of an approach which offers the potential to enable the prediction of the liquid-phase autoxidation and deposition of jet fuels. A chemical kinetic mechanism developed previously is refined to include the roles of key fuel species classes, such as phenols, reactive sulfur species, dissolved metals, and hydroperoxides. The concentrations of these fuel species classes are determined for the unreacted fuel samples and used as an input to the mechanism. The resulting model is used to simulate the autoxidation behavior observed over a range of fuel samples. The model includes simulation of the consumption of dissolved oxygen, as well as the formation and consumption of hydroperoxide species during thermal exposure. In addition, the chemical kinetic mechanism is employed with a global deposition submechanism in computational fluid dynamics (CFD) simulations of deposit formation occurring in near-isothermal as well as non-isothermal flowing environments.

Experimental Details

Both laminar and turbulent flow conditions can occur during aircraft fuel system operation. Under laminar flow conditions, the low flow rates result in relatively long residence times and slower rates of species and heat transport relative to those occurring in turbulent flow. Thus, it is important to perform experiments under both laminar and turbulent flow conditions to develop and validate models of oxidation and deposition. Two experimental rigs were used in the present work. The first rig, a near-isothermal flowing tube reactor (NIFTR), involved laminar flow and was used to evaluate the oxidation and deposition characteristics of seven jet fuels. The second rig employed turbulent flow and is a single-tube, non-isothermal flowing reactor system referred to as the ECAT.

The NIFTR system consists of a single-tube heat exchanger (32 in. length, 0.125 in. o.d., 0.085 in. i.d.) which has been described in detail previously.[11] Fuels are exposed to a temperature of 185 °C at 300 psig for all NIFTR experiments in the present work. The constant wall temperature provided by the copper block heater, along with low flow rates, provides a near-isothermal reaction environment for the fuel. In the oxidation experiments, where the oxygen consumption is monitored at various residence times, flow rates are varied over the range 0.25−5.0 mL min^{-1} (Reynolds numbers of 10−205 at the tube exit) using a syringe pump. Average residence times are calculated using the known reactor tube volume, flow rates, and a correction for fuel expansion with temperature. Oxygen profiles (dissolved oxygen fraction vs residence time) are determined by in-line sampling of the fuel and injection to a gas chromatographic system and are reproducible to ±5%.[12] Hydroperoxide profiles (hydroperoxide concentration vs residence time) are determined by reaction of collected fuel sample aliquots with triphenylphosphine, and quantification of the triphenylphosphine oxide produced via gas chromatography.[13] The oxidation experiments are performed using tubes coated with Silcosteel (Restek Corp.) to minimize surface catalysis and changes in fuel oxidation rates due to surface fouling if bare metal tubes were employed. Surface deposition is measured in separate 72 h runs utilizing the NIFTR system with a continuous flow rate of 0.25 mL min^{-1}. Uncoated stainless steel (SS316) tubes are used for the deposition experiments, with deposits produced during the first 10−12 h providing a noncatalytic surface for the vast majority of the test time. At the end of each deposition experiment, the tube is segmented into 2 in. long sections. The segments are washed with hexane to remove any residual fuel and, then, dried in a vacuum oven at 100 °C for at least 2 h. The total carbon deposition within each tube segment is then determined using standard carbon burnoff methods (LECO RC-412 Multiphase Carbon Determinator).

The deposition characteristics of one fuel, F4177, are also evaluated in a non-isothermal flowing environment utilizing the ECAT. A detailed description of the design and operation of the ECAT flow reactor system was presented in previous studies.[14−16] A single-tube Lindberg furnace is used to provide the heated reaction zone during testing. The furnace has a 36 in. actively heated zone with 5.25 in. insulating adapters at each end. Stainless steel tubing (SS316, 50 in. length, 0.125 in. o.d., 0.085 in. i.d.) is used for the ECAT deposition experiments. The tubing is positioned horizontally such that the 8−44 in. section is within the actively heated zone. Outer wall temperatures are monitored using thermocouples that are strap welded to the wall at various axial locations. The bulk fuel outlet temperature is measured using a thermocouple that is inserted into the fuel flow approximately 7 in. downstream of the heated reaction zone. Three ECAT deposition experiments at varying temperatures were performed, each with a fuel flow rate of 10 mL min^{-1} and system pressure of 550 psig. This flow rate for the fuel temperatures considered translates to Reynolds numbers in the range of 780−1000 at the tube exit. Such Reynolds numbers usually correspond to laminar flow. However, for the flows in the present heated horizontal tubes, buoyancy was assumed to prematurely induce turbulent flow. Others have demonstrated a similar premature transition to turbulence within horizontal heated tubes.[17] In addition, Katta et al.[18] have used this assumption to simplify simulations of the flow within heated horizontal tubes while providing good agreement between measured and calculated exit bulk temperatures. Thus in the simulations of the ECAT experiments, we assumed the flow to be turbulent. Upon completion of the 6 h of reaction time, the tubing is removed from the system and segmented, rinsed, and dried in a manner consistent with that previously described for the NIFTR deposition experiments. The total carbon deposition in each segment is measured using standard carbon burnoff methods. Table 1 provides a summary of the conditions of the NIFTR and ECAT jet fuel deposition experiments discussed in this work. The techniques used to quantify species class composition of the fuels are detailed in the following section.

Methodology

Jet fuels are comprised of hundreds, or perhaps thousands, of chemical species. The composition of a typical jet fuel is

(8) Doungthip, T.; Ervin, J. S.; Zabarnick, S.; Williams, T. F. *Energy Fuels* **2004**, *18*, 425−437.
(9) Ervin, J. S.; Zabarnick, S. *Energy Fuels* **1998**, *12*, 344−352.
(10) Doungthip, T. Ph.D. Thesis, University of Dayton, Dayton, OH, 2004.
(11) Jones, E. G.; Balster, L. M.; Balster, W. J. *Energy Fuels* **1998**, *12*, 990−995.
(12) Rubey, W. A.; Striebich, R. C.; Tissandier, M. D.; Tirey, D. A.; Anderson, S. D. *J. Chromatogr. Sci.* **1995**, *33*, 433−437.
(13) West, Z. J.; Zabarnick, S.; Striebich, R. C. *Ind. Eng. Chem. Res.* **2005**, *44*, 3377−3383.
(14) DeWitt, M. J.; Zabarnick, S. *Prepr. Pap.—Am. Chem. Soc., Div. Pet. Chem.* **2002**, *47*, 183−186.
(15) Minus, D. K.; Corporan, E. *Prepr. Pap.—Am. Chem. Soc., Div. Pet. Chem.* **2000**, *45*, 484−487.
(16) Minus, D. K.; Corporan, E. *Prepr. Pap.—Am. Chem. Soc., Div. Pet. Chem.* **1998**, *43*, 360−363.
(17) Kakac, S.; Shah, R.; Aung, W. *Handbook of Single-Phase Convective Heat Transfer*; Wiley-Interscience: New York, 1987.
(18) Katta, V. R.; Blust, J.; Williams, T. F.; Martel, C. R. *J. Thermophys. Heat Transfer* **1995**, *9*, 159−168.

Table 1. Summary of Deposition Experiments

	(a)	(b)
test rig	NIFTR	ECAT
no. experiments	7	3
Jet-A-1 fuels	F2747	N/A
Jet-A fuels	F2959, F3084, F3166, F3219	N/A
JP-8 fuels	F3804, F4177	F4177
tubing type	stainless steel (SS316)	stainless steel (SS316)
tube o.d.	0.125 in.	0.125 in.
tube i.d.	0.085 in.	0.085 in.
tube length	32 in.	50 in.
tube orientation	horizontal	horizontal
flow rate	0.25 mL min^{-1}	10.0 mL min^{-1}
flow pressure (inlet)	2.3 MPa	3.9 MPa
inlet temperature	room temperature	room temperature
wall temperature	constant (185 °C)	variable (21−400 °C), maximum wall temps of 340, 370, and 400 °C
active heating	0−32 in. section of tubing	8−44 in. section of tubing
exit temperature	185 °C	300−355 °C
exit Reynolds nos.	10	780−1000
test duration	72 h	6 h

approximately 80% alkanes, 10−25% alkylated aromatics, and parts per million to parts per thousand quantities of heteroatomic species. The heteroatomic species consist of oxygen-containing molecules, such as phenols and hydroperoxides; sulfur-containing molecules, such as thiols, sulfides, disulfides, benzothiophenes, dibenzothiophenes, and elemental sulfur; and, lastly, nitrogen-containing molecules, such as anilines, pyridines, indoles, amines, and carbazoles. Although the heteroatomic species represent less than 1% of the typical fuel content, they are the primary species responsible for differences among oxidation and deposition behavior of fuel samples. As all of the species in jet fuel may contribute to jet fuel oxidation and deposition behavior to some degree, ideally it would be desirable to identify and quantify them individually and to understand how they affect oxidation and deposition processes. Unfortunately, due to the complex mixture that constitutes jet fuel and the variation between fuel samples (which are specified via properties rather than chemical composition), it is impractical to consider the detailed concentrations and reactions of hundreds of varying species. Therefore, the oxidation and deposition behavior of jet fuel has been characterized in a pseudo-detailed (i.e., simplified) chemical kinetic mechanism in which the fuel is treated as a mixture of classes of compounds, rather than individual species. Thus, the relevant species classes need to be identified, quantified, and incorporated into a reaction mechanism which includes the chemical behavior of interest.

Chemical Kinetic Mechanism. The basic autoxidation mechanism has been described in detail previously[4−6] and is shown schematically in Figure 1. The mechanism is limited to the most important reactions in determining fuel oxidation behavior. The species classes represented in the cycle are: hydrocarbons (RH), dissolved oxygen (O_2), peroxy radical inhibitors or antioxidants (AH), hydroperoxide decomposers (SH), and hydroperoxides (ROOH). The cycle begins with a poorly understood initiation process that produces a hydrocarbon radical, R•. The resultant radical reacts rapidly with dissolved oxygen, forming a peroxy radical, RO_2•. This peroxy radical can extract a hydrogen atom from a fuel hydrocarbon (likely an alkyl-substituted aromatic species), forming a hydroperoxide and regenerating the R• radical, thereby continuing the cycle. Due the reactivity of benzylic hydrogen atoms relative to those in paraffinic species, the hydrocarbon radical, R•, which propagates the chain is likely a benzylic radical.[19] This process

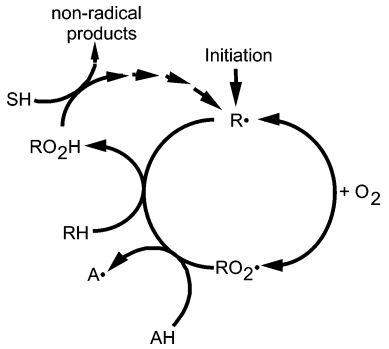

Figure 1. Diagram of the autoxidation reaction process showing the role of peroxy radical inhibiting (AH) and hydroperoxide decomposing (SH) species classes.

Table 2. Chemical Kinetic Mechanism of Liquid-Phase Oxidation

#	reaction	A (mol, L, s)	E_a (kcal mol^{-1})
1	I → R•	1×10^{-3}	0
2	R• + O_2 → RO_2•	3×10^{9}	0
3	RO_2• + RH → RO_2H + R•	3×10^{9}	12
4	RO_2• + RO_2• → termination	3×10^{9}	0
5	RO_2• + AH → RO_2H + A•	3×10^{9}	5
6	A• + RH → AH + R•	1×10^{5}	12
7	A• + RO_2• → $Products_{AH}$	3×10^{9}	0
8	R• + R• → R_2	3×10^{9}	0
9	RO_2H → RO• + •OH	1×10^{15}	39
10	RO• + RH → ROH + R•	3×10^{9}	10
11	RO• → R_{prime}• + carbonyl	1×10^{16}	15
12	•OH + RH → H_2O + R•	3×10^{9}	10
13	RO• + RO• → RO_{term}•	3×10^{9}	0
14	R_{prime}• + RH → alkane + R•	3×10^{9}	10
15	RO_2H + SH → $Products_{SH}$	3×10^{9}	18
16	RO_2• → R• + O_2	1×10^{16}	19
17	RO_2• + R• → termination	3×10^{9}	0
18	RO_2H + M → RO• + •OH + M	3×10^{10}	15

can be slowed by the presence of antioxidant species, AH, which can be naturally occurring fuel species or added synthetic antioxidants. These species intercept the peroxy radical, slowing the chain by preventing the reformation of hydrocarbon radicals. The presence of hydroperoxide decomposing species, SH, can also slow the oxidation of the fuel. These species slow oxidation by decomposing hydroperoxides via a nonradical-producing pathway. Hydroperoxides act as initiators in the mechanism, increasing the free radical pool and the resulting oxidation rate. Thus, at temperatures where the oxidation rate is being influenced by hydroperoxide initiation, the removal of hydroperoxides results in a reduction of the oxidation rate.[20]

The chemical kinetic mechanism and associated Arrhenius rate parameters describing the basic autoxidation cycle of Figure 1 have been previously published.[6] The enhanced version used in the present work is shown in Table 2. Use of the mechanism to model individual fuel samples requires analytical techniques to quantify the important species classes, AH, SH, and ROOH, as well as dissolved metals (denoted as M in Table 2). Techniques used for the identification and quantification of these species classes, as well as evidence of their involvement in fuel autoxidation and deposition, are now presented.

AH Species Class. There is much evidence indicating that polar species, and phenols which comprise the bulk of the jet fuel polars, play an important role in determining the oxidation and deposition characteristics of fuel samples. Phenols are known to act as antioxidants in hydrocarbons[21] and have been shown to slow oxidation in jet fuel samples.[22,23] It is known

(19) Zabarnick, S.; Phelps, D. K. *Energy Fuels* **2006**, *20*, 488−497.
(20) Zabarnick, S.; Mick, M. S. *Ind. Eng. Chem. Res.* **1999**, *38*, 3557−3563.

Table 3. Polar, Hydroperoxide, and Reactive Sulfur Content of the Seven Fuels Studied

fuel sample	polars concentration (relative)[a]	polars concentration (mg L^{-1})[b]	hydroperoxides conc (μM)	reactive sulfurs conc (ppmwt)
F2747 (Jet A-1)	0.32	167	21	1
F2959 (Jet A)	0.43	222	3	911
F3084 (Jet A)	0.90	465	13	426
F3166 (Jet A)	1.00	515	11	519
F3219 (Jet A)	0.43	223	5	286
F3804 (JP-8)	0.34	177	21	366
F4177 (JP-8)	0.94	486	13	1069

[a] Integral of 254 nm UV response obtained using the normal-phase HPLC method for polar species quantification[25] divided by that obtained for fuel F3166. [b] Estimate of absolute polar concentrations based on phenol calibration mixture studies.[32]

from the experience gained studying many fuel samples that jet fuels with high concentrations of naturally present phenol species tend to oxidize slowly and jet fuels with low concentrations of these phenols tend to oxidize quickly.[24] In addition to having important effects on oxidation, there is also evidence which suggests that phenols have significant effects on surface deposition. For example, the deposits produced over a wide range of fuel samples have been correlated with measured concentrations of polar fuel fraction,[25] and the removal of polar phenols via solid-phase extraction[26] or silylation[27] results in increased oxidation rates and decreased deposition. In addition, experiments in blending jet fuels with solvents, which is a method to decrease the concentration of these species in the fuels, also suggest the involvement of phenols in slowing oxidation and increasing deposition.[28,29] These observations provide compelling evidence that naturally occurring phenols are responsible for slowing oxidation and causing deposition in jet fuels.

A number of techniques have been developed to measure polar fuel species. These species can be separated and quantified by normal-phase HPLC with UV absorption detection.[25] Solid-phase extraction techniques using silica gel cartridges can also separate these fuel components which can be subsequently quantified by gas chromatography.[30] In addition, liquid−liquid extraction followed by chromatographic analysis has also been employed.[31] While hydrocarbon fuel polars may consist of a number of species classes, for jet fuels the polars have been found to consist mostly of phenolic species.[32] For example, analysis of the polar fraction of jet fuels via silica gel solid-phase extraction yielded a series of alkyl-substituted phenols almost exclusively.[30] The concentration of polar species determined by the normal-phase HPLC method is shown in Table 3 for the seven fuels studied here. The table shows that the polar concentrations in these fuels cover the range 167−515 mg L^{-1}. Analysis of a wide range of jet fuel samples indicates that the vast majority contain from 100 to 600 mg L^{-1} of polars.[32]

Use of the measured polar species class concentrations for numerical modeling purposes is complicated by the fact that various species measured within a class have a range of reactivities. For example, a given fuel sample may have many dozens of naturally occurring phenols, including methyl-substituted, dimethyl-substituted, and larger phenols. During fuel autoxidation each of these phenols is capable of intercepting peroxy radicals via,

$$RO_2^{\bullet} + AH \rightarrow RO_2H + A^{\bullet}$$

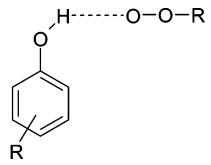

where AH is a phenol species and $A^{\bullet}$ is a phenoxy radical. The Arrhenius rate parameters of the reaction vary for different phenol species. In later sections, a method to relate the measured polar (phenol) species class concentration to the AH concentration used in the model is discussed.

SH Species Class. Another important class of species in fuel oxidation and deposition are those species which react with fuel hydroperoxides via a nonradical-producing pathway. Alternatively, hydroperoxides can decompose thermally or catalytically to produce radicals which accelerate the autoxidation chain. In jet fuels, these nonradical-producing hydroperoxide decomposing species include a subset of sulfur compounds, such as sulfides and disulfides. These can react with hydroperoxides via

$$\text{ROOH} + \text{RSR} \rightarrow \text{ROH} + \text{sulfoxide}$$

$$\text{ROOH} + \text{RSSR} \rightarrow \text{ROH} + \text{thiosulfinate}$$

where RSR is a sulfide and RSSR is a disulfide. These sulfur-containing species are referred to as "reactive sulfur" to differentiate them from the relatively unreactive thiophenes, benzothiophenes, and dibenzothiophenes that are commonly found in jet fuels. It has been shown in previous work that jet fuels which contain high levels of reactive sulfur species tend to produce only very low levels of hydroperoxides during autoxidation, while fuels with low levels of reactive sulfur species tend to produce relatively high levels of hydroperoxides.[28] Hydroperoxide-decomposing species serve to reduce the oxidation rate by reducing thermal or catalytic hydroperoxide decomposition and have been shown to act synergistically with peroxy radical inhibiting species in slowing oxidation.[20] Thus, the reactive sulfur species (sulfides and disulfides) are believed to be the primary components of the SH species class denoted in Figure 1. In addition to affecting oxidation, there is also evidence that oxidizable sulfur compounds promote surface deposition.[33] Thus, the reactive sulfur species (sulfides and disulfides) may also contribute to deposit formation.

A hydroperoxide reaction technique is used to quantify these reactive sulfur species in fuel.[34,35] Fuels are reacted with hydrogen peroxide and/or iodine and the remaining sulfur

(21) Taylor, W. F.; Frankenfeld, J. W. *Ind. Eng. Chem. Prod. Res. Dev.* **1978**, *17*, 86−90.
(22) Zabarnick, S.; Whitacre, S. D. *J. Eng. Gas Turbines Power* **1998**, *120*, 519−525.
(23) Jones, E. G.; Balster, L. M. *Energy Fuels* **2000**, *14*, 640−645.
(24) Heneghan, S. P.; Zabarnick, S. *Fuel* **1994**, *73*, 35−43.
(25) Balster, L. M.; Zabarnick, S.; Striebich, R. C. *Prepr. Pap.—Am. Chem. Soc., Div. Pet. Chem.* **2002**, *47*, 161−164.
(26) Zabarnick, S. *Ind. Eng. Chem. Res.* **1994**, *33*, 1348−1354.
(27) Zabarnick, S.; Mick, M. S.; Striebich, R. C.; Grinstead, R. R. *Energy Fuels* **1999**, *13*, 154−159.
(28) Jones, E. G.; Balster, W. J.; Balster, L. M. *Energy Fuels* **1996**, *10*, 509−515.
(29) Zabarnick, S.; Zelesnik, P.; Grinstead, R. R. *J. Eng. Gas Turbines Power* **1996**, *118*, 271−277.
(30) Zabarnick, S.; Striebich, R.; Straley, K.; Balster, L. *Prepr. Pap.—Am. Chem. Soc., Div Pet. Chem.* **2002**, *47*, 223−226.
(31) Link, D. D.; Baltrus, J. P.; Zandhuis, P.; Hreha, D. C. *Energy Fuels* **2005**, *19*, 1693−1698.
(32) Balster, L. M.; Zabarnick, S.; Striebich, R. C.; Shafer, L. M.; West, Z. J. *Energy Fuels* **2006**, *20*, 2564−2571.
(33) Kauffman, R. E. *J. Eng. Gas Turbines Power* **1997**, *119*, 322−327.
(34) Stumpf, A.; Tolvaj, K.; Juhasz, M. *J. Chromatogr., A.* **1998**, *819*, 67−74.
(35) Link, D. D.; Baltrus, J. P.; Rothenberger, K. S.; Zandhuis, P.; Minus, D. K.; Striebich, R. C. *Energy Fuels* **2003**, *17*, 1292−1302.

species are quantified by gas chromatography with atomic emission detection. As iodine only reacts with mercaptan sulfur, the mercaptan level can be determined by subtraction. Hydrogen peroxide reacts with sulfides, disulfides, and mercaptans, so that the sulfide plus disulfide level can be determined by subtraction and the use of the previously determined mercaptan level. These techniques show that jet fuels usually have very low mercaptan levels (<5 ppmwt) and the levels of reactive sulfur, i.e., sulfide plus disulfide classes, typically vary over the range 0−1000 ppmwt. The concentrations of reactive sulfur determined for the seven fuels of the present work are shown in Table 3. Use of the measured reactive sulfurs for numerical modeling is also complicated by the fact that various species measured within the class have a range of reactivities. Again, various sulfides and disulfides react with hydroperoxides at different rates, and the measured reactive sulfur content of the fuel needs to be related to the SH concentration used in the model.

ROOH Species Class. Hydroperoxides are important species in fuel oxidation which greatly affect the overall oxidation rate. These highly reactive species are usually present at only very low concentrations. Hydroperoxides are produced and destroyed during fuel autoxidation but also exist in fuel prior to thermal exposure. A technique to quantify fuel hydroperoxides as a species class using reaction with triphenylphosphine via

$$\mathrm{ROOH} + \mathrm{TPP} \rightarrow \mathrm{ROH} + \mathrm{TPPO}$$

has recently been developed.[13] The triphenylphosphine oxide (TPPO) produced is quantified by gas chromatography. This technique uses small sample volumes (≤0.5 mL), has a low detection limit (0.002 mM) and a wide dynamic range, and is fast, reproducible, and accurate. The small required sample volume allows laboratory-scale oxidation tests to be sampled readily for hydroperoxide content. The low detection limit allows the determination of hydroperoxide levels in fuels prior to thermal exposure. As various fuel hydroperoxides have very similar reactivity, this measurement of the hydroperoxide content of the unstressed fuel can be used directly as an input to the kinetic mechanism. We find that most fuels have hydroperoxide concentrations of 3−30 μM. Results on the hydroperoxide content of the seven fuels studied here are shown in Table 3. Kinetic analysis shows that at 185 °C, thermal decomposition (via reaction 9 of Table 2) of these low levels of hydroperoxides creates a radical pool which is sufficient to initiate the autoxidation chain. Thus, reaction 1 of Table 2, which is used to create an artificial source of radical production to start the autoxidation chain, is unnecessary but is still used in the present modeling to retain consistency with previous work. Low levels of hydroperoxides, such as those found in jet fuels, may also be responsible for initiating autoxidation in other hydrocarbon oxidation systems.[36]

Dissolved Metals. Dissolved metals are known to play important roles in the oxidation and deposition of jet fuels.[2] Metals increase the decomposition rate of hydroperoxides via a catalytic pathway and may also provide catalysis of other reactions. It is essential to accurately quantify these species which can be active at very low concentrations (e.g., dissolved copper has been shown to be active at a concentration as a low as 25 ppb). Inductively coupled plasma (ICP) techniques with either atomic emission spectroscopy (AES) or mass spectrometric detection provide promising ways for their identification and quantitation. Metals concentrations via ICP-AES for the seven fuels of the present work are shown in Table 4. The metals

(36) Benson, S. W.; Nangia, P. S. *Acc. Chem. Res.* **1979**, *12*, 223−228.

Table 4. Dissolved Metal Content of the Seven Fuels Studied (via ICP-AES)

fuel	Cu (μg L^{-1})	Mn (μg L^{-1})	Fe (μg L^{-1})	Mg (μg L^{-1})	Zn (μg L^{-1})
F2747 (Jet A-1)	40	<10	93	33	89
F2959 (Jet A)	<18	58	174	34	153
F3084 (Jet A)	25	<10	142	34	101
F3166 (Jet A)	111	13	142	34	100
F3219 (Jet A)	58	<10	182	40	128
F3804 (JP-8)	<18	<10	196	29	131
F4177 (JP-8)	<18	88	144	26	69

quantified here (Cu, Mn, Mg, Fe, and Zn) were selected for their known ability to catalyze autoxidation or deposition, as well as their being commonly found in fuel samples. Other metals, such as vanadium, are known to be detrimental to fuel thermal stability but are not generally found in jet fuel distillate cuts. The table shows that Cu and Mn exhibit a wide variation in measured concentrations, from below the detection limit to over 100 μg L^{-1}, while Fe, Mg, and Zn display significantly less variability. All of the fuels contain measurable levels of Fe, Mg, and Zn. Fuels with high measurable amounts of Cu tend to have low Mn levels, while fuels with measurable amounts of Mn tend to have low Cu levels. Fe, Mg, and Zn usually affect fuel thermal stability only at levels greater than those found in these fuels.[2] For these reasons, in using the measured metals content in the kinetic mechanism, the Cu and Mn concentrations were employed in the current work. Future studies need to more closely examine the role and catalysis rates of various metal species present in fuels.

Incorporating Measured Species Class Concentrations into the Kinetic Model. Measurement of species concentrations as grouped species classes provides a way to characterize differences between fuel samples and begins to reveal why various fuel samples have varying oxidation rates and deposit forming tendencies. Above, justification was provided for using the measured polars (primarily phenols) concentration as the peroxy radical inhibiting species class, AH, as well as the measured sulfur species which react with hydroperoxides as the hydroperoxide decomposing species class, SH. Again, these species classes represent an ensemble of individual species with a range of reactivities, and as such, a means to incorporate these species class measurements into the kinetic mechanism is required. The relationship between measured species classes and the concentrations used in the model should ideally be proportional so that, for example, a doubling of the measured phenol content results in a doubling of the AH concentration used in the model. The approach taken here was to model the initial AH and SH concentrations via linear relationships which define constants of proportionality,

$$\mathrm{Const_{AH}} = \frac{\text{Simulated } \mathrm{AH_0[M]}}{\text{Measured polars[mg/L]}}$$

$$\mathrm{Const_{SH}} = \frac{\text{Simulated } \mathrm{SH_0[M]}}{\text{Measured reactive sulfurs[ppmwt]}}$$

between fuel species class composition measurements and simulated initial concentrations. Values of these constants are constrained such that the molar concentrations employed in the kinetic mechanism are less than or equal to the molar concentrations of the measured species classes. This constraint derives from the selection of Arrhenius parameters for the more reactive members of the species class. For example, Arrhenius parameters for the peroxy radical reaction with phenols, reaction 5 in Table 2, were selected for very reactive phenolic species, such

as hindered phenols, but most naturally occurring fuel phenols are likely to be less reactive. Thus, the species class concentrations used in the model for AH and SH must be less than the measured species class concentrations.

For simplicity, dissolved metals were not included in previous pseudo-detailed chemical kinetic mechanisms of fuel oxidation. To assess the relative importance of dissolved metals in influencing oxidation behavior in the present work, a single metal-catalyzed reaction is appended to the kinetic mechanism (reaction 18 of Table 2):

$$\mathrm{ROOH} + \text{dissolved metals} \rightarrow \mathrm{RO}^{\bullet} + {}^{\bullet}\mathrm{OH} + \text{dissolved metals}$$

This reaction increases the rate of hydroperoxide decomposition via a catalytic pathway but is a simplification of the complex chemistry associated with dissolved metal catalysis in a number of respects. For example, the varied reactivity of individual dissolved metals such as Cu and Mn which are known to catalyze hydroperoxide decomposition[37] is not included here. In addition, the reaction is a simplification of the steps that may be involved in the catalysis of hydroperoxide decomposition. Two-step redox schemes of the form

$$\mathrm{M}^{n+} + \mathrm{ROOH} \rightarrow \mathrm{M}^{(n+1)+} + \mathrm{RO}^{\bullet} + {}^{\bullet}\mathrm{OH}$$

$$\mathrm{M}^{(n+1)+} + \mathrm{ROOH} \rightarrow \mathrm{M}^{n+} + \mathrm{ROO}^{\bullet} + \mathrm{H}^{+}$$

have been proposed[38] for the catalytic decomposition of hydroperoxides involving dissolved metal ions with multiple oxidation states. However, recent studies utilizing density functional theory suggest that metal-catalyzed decomposition of hydroperoxides involves the formation of a complex and its subsequent decomposition to form radicals without regeneration of the metal ion.[19] Another simplification associated with using the above single reaction is the exclusion of other catalytic reaction pathways that may be important. That is, in addition to the catalytic decomposition of hydroperoxides, dissolved metals may catalyze fuel oxidation and deposition via other reaction pathways. In addition, the single-step reaction cannot truly be catalyzed by metals, as the thermal hydroperoxide decomposition reaction is known to not contain a barrier.[19] While the single catalysis reaction is a simplification of the poorly understood metal catalysis process, its inclusion in the mechanism provides a relatively simple method to assess the importance of metal catalysis in jet fuel autoxidation and deposition.

The mechanism of Table 2 also employs a refined set of reactions for peroxy radical inhibition compared to previous studies.[4−6] These reactions (reactions 6 and 7 of Table 2),

$$\mathrm{A}^{\bullet} + \mathrm{RH} \rightarrow \mathrm{AH} + \mathrm{R}^{\bullet}$$

$$\mathrm{A}^{\bullet} + \mathrm{RO_2}^{\bullet} \rightarrow \mathrm{Products_{AH}}$$

replace a series of reactions which begin with reaction of $\mathrm{A}^{\bullet}$ with O_2 in the previous mechanism. As phenoxy radicals do not readily react with O_2, the previous mechanism is incorrect for phenol type AH species. The previous work employed reactions which represented AH species more broadly as the many different species capable of reacting with peroxy radicals, as opposed to the current work where the AH species class is being associated with phenol species only. These new reactions have $\mathrm{A}^{\bullet}$ reacting with the fuel species RH or terminating with an RO_2 radical. In addition to more closely representing the important reactions which occur in this system, the new reactions provide improved agreement for the hydroperoxide profiles reported below.

Numerical Simulations. All chemical kinetic simulations presented here were performed using the LSODA solver[39] to integrate the multiple differential equations defined by the reaction mechanisms considered in a manner consistent with Whitbeck's methodology[40] for chemical kinetic simulations. It is important to note that these simulations do not solve the energy equation, so temperature changes due to exothermic or endothermic reactions are not modeled. At the relatively low temperature autoxidation conditions and low levels of dissolved oxygen considered here, energy changes should not be large enough to significantly affect the fuel temperature. In addition to individual chemical reactions and their associated rate parameters (A and E_a), the initial species concentrations for all species are required as inputs along with the reaction time, temperature, and tolerances for precision of the LSODA integration. Initial concentrations of $[\mathrm{I}]_0 = 1 \times 10^{-8}$ M, $[\mathrm{O_2}]_0 = 1.8 \times 10^{-3}$ M, and $[\mathrm{RH}]_0 = 4.7$ M are used for all simulations of the present work. Individual fuel samples are modeled via initial concentrations of polar species ($[\mathrm{AH}]_0$), reactive sulfurs ($[\mathrm{SH}]_0$), hydroperoxide species ($[\mathrm{ROOH}]_0$), and dissolved metals ($[\mathrm{M}]_0$). The concentrations employed in the model for these species for each of the seven fuel samples are discussed in later sections. The initial concentrations of all remaining species in the mechanism are modeled as zero. The output for the kinetic simulations is concentration versus time for all species present in the reaction mechanism.

The computational fluid dynamics (CFD) simulations presented here were performed utilizing the commercially available FLUENT software package (Fluent, Inc., Lebanon, NH). The fuel flow within the tubing of the deposition experiments was assumed to be axisymmetric and steady. Thus, the conservation equations that are solved here may be expressed as

$$\frac{\partial(\rho V_z \Phi)}{\partial z} + \frac{\partial(\rho V_r \Phi)}{\partial r} = \frac{\partial}{\partial z}\left(\Gamma^{\Phi}\frac{\partial \Phi}{\partial z}\right) + \frac{\partial}{\partial r}\left(\Gamma^{\Phi}\frac{\partial \Phi}{\partial r}\right) - \frac{\rho V_r \Phi}{r} + \frac{\Gamma^{\Phi}}{r}\frac{\partial \Phi}{\partial r} + S^{\Phi}$$

In this equation, ρ is the fuel density, V_r is the radial velocity component, V_z is the axial velocity component, r represents a radial coordinate, and z represents an axial coordinate. Table 5 provides a list of the transport coefficients (Γ^{Φ}) and source terms (S^{Φ}) corresponding to solution variables represented by Φ. In Table 5, c_p is the specific heat, κ is the thermal conductivity, and μ is the absolute viscosity. The variables k, ϵ, h, P, and Y_i are the turbulent kinetic energy, its dissipation, enthalpy, pressure, and the mass fraction of species i, respectively. D is the diffusion coefficient, M_{Wi} is the molecular weight of species i, and $M_{Wi}\sum_{j=1}^{N_R} R_{i,j}$ is the rate of production. All simulations incorporate relationships describing the temperature dependence of fuel properties (density, thermal conductivity, specific heat, and absolute viscosity). The relationships used are based on curve fits of fuel property data.[41] Here, we simulate the rate of initial surface deposition. The presence of the time-

(37) Syroezhko, A. M.; Begak, O. Y. *Russ. J. Appl. Chem.* **2004**, *77*, 1301−1307.

(38) Walling, C. *Free Radicals in Solution*; John Wiley & Sons: New York, 1957.

(39) Radhakrishnan, K.; Hindmarsh, A. C. 1993, UCRL-ID-113855.

(40) Whitbeck, M. *Tetrahedron Comput. Methodol.* **1990**, *3*, 497−505.

(41) Nixon, A. C.; Ackerman, G. H.; Faith, L. E.; Henderson, H. T.; Ritchie, A. W. 1967, AFAPL-TR-67-114.

Table 5. Transport Coefficients and Source Terms Appearing in Steady-State Axisymmetric Conservation Equation[a]

Φ	Γ^{Φ}	S^{Φ}
1	0	0
Y_i	$\rho D + \frac{\mu_t}{\sigma_{Yi}}$	$M_{Wi}\sum_{j=1}^{N_R} R_{i,j}$
h	$\frac{k}{c_p} + \frac{\mu_t}{\sigma_h}$	0
V_r	$\mu + \mu_t$	$-\frac{\partial P}{\partial r} + \frac{\partial}{\partial z}\left(\Gamma^{\Phi}\frac{\partial V_z}{\partial r}\right) + \frac{\partial}{\partial r}\left(\Gamma^{\Phi}\frac{\partial V_r}{\partial r}\right) + \frac{\Gamma^{\Phi}}{r}\frac{\partial V_r}{\partial r} - 2\Gamma^{\Phi}\frac{V_r}{r^2}$
V_z	$\mu + \mu_t$	$-\frac{\partial P}{\partial z} + \frac{\partial}{\partial z}\left(\Gamma^{\Phi}\frac{\partial V_z}{\partial z}\right) + \frac{\partial}{\partial r}\left(\Gamma^{\Phi}\frac{\partial V_r}{\partial z}\right) + \frac{\Gamma^{\Phi}}{r}\frac{\partial V_r}{\partial z}$
k	$\mu + \frac{\mu_t}{\sigma_k}$	$G - \rho\epsilon$
ϵ	$\mu + \frac{\mu_t}{\sigma_\epsilon}$	$C_{1\epsilon}G\frac{\epsilon}{k} - C_{2\epsilon}\rho\frac{\epsilon^2}{k}$

[a] $\mu_t = \rho C_\mu \frac{k^2}{\epsilon}$

$G = \mu_t\left\{2\left[\left(\frac{\partial V_z}{\partial z}\right)^2 + \left(\frac{\partial V_r}{\partial r}\right)^2 + \left(\frac{V_r}{r}\right)^2\right] + \left[\left(\frac{\partial V_r}{\partial z}\right) + \left(\frac{\partial V_z}{\partial r}\right)\right]^2\right\}$

$C_{1\epsilon} = 1.44$, $C_{2\epsilon} = 1.92$, $C_\mu = 0.09$, $\sigma_k = 1.0$, $\sigma_\epsilon = 1.3$, $\sigma_{Yi} = 0.70$, $\sigma_h = 0.85$.

evolving surface deposits on the flow and heat transfer was not included in the simulations.

For NIFTR CFD simulations, a constant wall temperature boundary condition of 185 °C is prescribed. The flow is assumed to be laminar within the NIFTR tubing based on previous analysis of the flowfield under similar experimental conditions.[8] A uniformly spaced computational grid of 180 axial elements by 15 radial elements is used to model the axisymmetric geometry. Analysis of the effects of grid resolution on the simulated centerline temperature in the entry region of the NIFTR tubing was used as a basis for determining required grid resolution. Simulations of the centerline temperature in the NIFTR experiments indicate that the temperature is isothermal over more than 90% of the tubing length. This result has important ramifications in later analyses of chemical reactions occurring in the flowfield and along the wall boundary.

For ECAT CFD simulations, a fit of the measured outer wall temperatures is used to prescribe an axially varying temperature profile along the flowfield outer boundary (interior wall). As the tube wall is thin (0.02 in. thickness), the radial temperature gradient between the outer and inner wall is not modeled for simplicity. The flow is modeled as turbulent within the ECAT tubing based on previous flowfield analysis of non-isothermal experiments performed with the same tubing at similar flowrates. A standard $k-\epsilon$ turbulence model is used. A uniformly spaced computational grid of 360 axial elements by 30 radial elements is used to model the axisymmetric geometry. Analysis of the effects of grid resolution on simulated mass-averaged bulk exit temperatures over the range of ECAT experiments was used as a basis for determining the required grid resolution. The simulated bulk exit temperatures (not shown) are within 1% of the measurements for all experiments.

Results and Discussion

Chemical Kinetic Modeling of Fuel Oxidation. A series of thermal oxidative test runs were performed on seven fuel samples to generate an experimental data set suitable for evaluation of the role of the species classes discussed above in the autoxidation mechanism. NIFTR experiments were conducted at 185 °C on each of the seven fuels, and dissolved oxygen and hydroperoxide concentrations were measured as a function of flow rate (i.e., at varying residence time). This temperature was selected as representative of the highest temperatures of fuel exposure in aircraft fuel system engine nozzles, where deposition is most problematic. Flow rate ranges were selected so that the complete oxygen consumption profile would be measured. As each fuel experiment is performed under identical conditions, the variances in oxidation behavior observed are due to chemical composition differences between the fuels. Figure 2 shows the dissolved oxygen consumption profiles of the seven fuels in these NIFTR experiments. The figure shows that the dissolved oxygen consumption rates of the fuel samples vary by almost an order of magnitude, with complete oxygen consumption times ranging from ~1.5 to almost 9 min. The observed differences in oxidation rates are due to the varied species class compositions of the fuels. Fuel-like hydrocarbon mixtures with essentially zero heteroatom and metals content, such as Exxsol D80, display very fast oxidation curves with complete oxygen consumption in <1 min.[42] The slower oxidation rates observed for these fuels are due to the

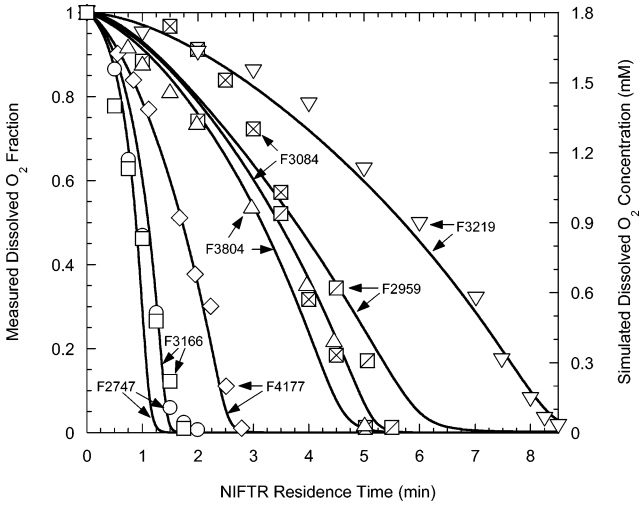

Figure 2. Comparison of measured and simulated dissolved oxygen consumption for seven fuels stressed at 185 °C. Symbols denote measurements. Curves denote chemical kinetic simulations.

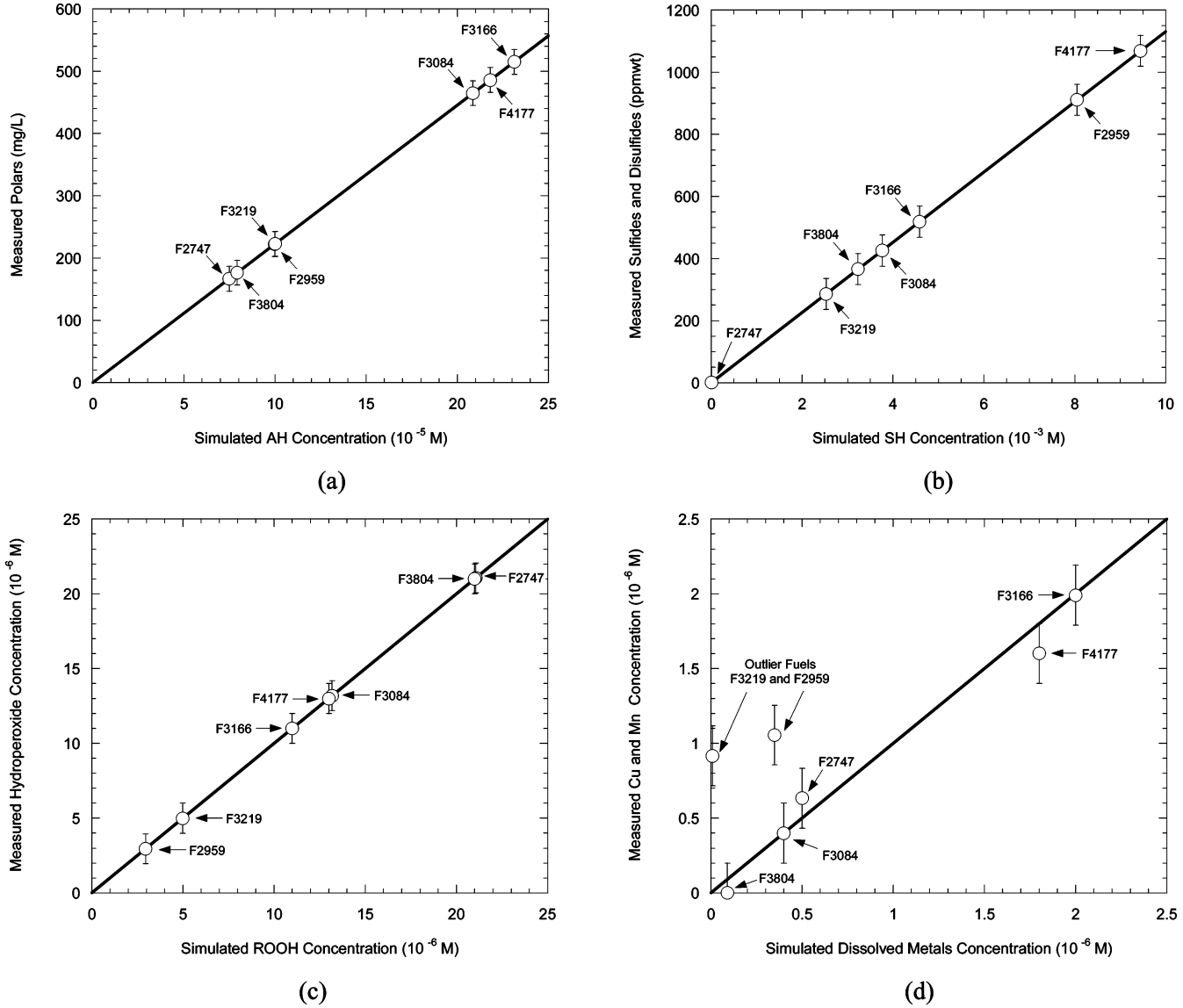

Figure 3. Plots of measured concentrations for various species classes vs concentrations used to model fuel samples in numerical simulations: (a) polars vs AH; (b) reactive sulfurs vs SH; (c) hydroperoxides vs ROOH; (d) dissolved metals (Cu + Mn) vs M.

presence of species that slow the autoxidation chain. The curved lines in Figure 2 are chemical kinetic simulations for each of the fuels. The figure shows that very good agreement between the measured oxidation profiles and the modeled profiles were obtained for all seven fuels. The kinetic modeling results reported here utilize the mechanism of Table 2 for each of the fuels. The mechanism and Arrhenius parameters employed were not adjusted for the different fuel samples, rather, the AH, SH, ROOH, and metals species class input concentrations to the model were different for each fuel. The relationships developed between the measured species class concentrations (Tables 3 and 4) and initial concentrations input to the model for these species classes are shown in Figure 3. The figure shows that proportional relationships were used for the peroxy radical inhibiting (AH) and hydroperoxide decomposing (SH) species classes and that the measured hydroperoxide concentrations were used directly in the model. A proportional relationship in metals content did not allow good agreement for all seven fuels with the measured oxygen profiles. Figure 3 shows that for the metals species a proportional relationship only holds for five of the seven fuels; for two of the fuels (F3219 and F2959), agreement with the oxidation curves could only be obtained if lower concentrations of metal content than the measured values were employed. Further study of the metals content of these fuels was performed to determine the cause of this discrepancy.

The concentrations of dissolved metals found in the seven fuels is summarized in Table 4. As stated above, only the Cu and Mn concentrations were employed in the model, as the concentrations of the other metals do not differ appreciably among the various fuels. In addition, it is known that Cu and Mn play a role in catalysis of hydroperoxide decomposition[37] and that Fe, Mg, and Zn are thought to affect fuel oxidation and deposition only at higher levels.[2] It was hypothesized that if some of the fuels contained metal deactivator additive (MDA), this could be inhibiting the catalytic activity of the metal and result in a nonproportional modeling relationship. If MDA is present in a fuel, the metal activity would be reduced, resulting in a measured metal content which is too high for use in the model. Ultimately, it is desirable to measure only metals which are not complexed with MDA and thus available for catalytic activity, but the standard ICP analysis yields the total metals content of each metal (i.e., both complexed and uncomplexed

(42) Balster, L. M.; Balster, W. J.; Jones, E. G. *Energy Fuels* **1996**, *10*, 1176−1180.

metals). To address this hypothesis, MDA analyses[43] of each of the fuels was performed, which yielded measurable uncomplexed MDA in fuel F3219 only (the technique employed only responds to uncomplexed MDA). This is one of the two outlier fuels in the metals plot of Figure 3. Finding uncomplexed MDA in this fuel indicates that this fuel contains excess MDA and that all metal species are likely complexed. Thus, the metals concentration used in the model for this fuel should be zero or very low, which is precisely where the F3219 data point needs to be to fall on the $y = x$ line shown in the metals plot of Figure 3. Thus, MDA can account for the first outlier fuel in the metals plot. MDA was not detected in the second outlier fuel (F2959), but again, the analysis technique employed only measures uncomplexed MDA. The metals plot of Figure 3 suggests that for fuel F2959, while MDA may be present, its concentration is not high enough to complex all the metal species present, and thus, an excess of uncomplexed MDA would not be expected. These results indicate that techniques need to be developed to quantify "reactive metals", i.e., dissolved metals in the fuel that are actively involved in catalysis reactions. Unfortunately, most metal analysis techniques do not distinguish between inactive (e.g., complexed with MDA) and active (or reactive) metals. One promising method which is able to provide this differentiation uses HPLC to separate the metals species, with flame atomic absorption detection of the metal atoms.[44,45]

While being able to simulate the dissolved oxygen consumption of seven fuels using measured species classes shows that the kinetic mechanism and species class method is promising, a more stringent evaluation is provided by comparing the simulated and measured changes in hydroperoxide concentrations that occur during thermal stressing. These results are shown in Figure 4. The hydroperoxide quantities produced vary by over an order of magnitude for the seven fuels, ranging from ~0.05 (F3804) to ~1.3 mM (F2747). In addition, the residence times of the peak hydroperoxide concentration vary substantially from ~1.3 min (F3166) to fuels for which the hydroperoxide concentration is still increasing at 7 min (e.g., F3219). This varied behavior reflects the different quantities of species involved in the production and destruction of hydroperoxides for each fuel. Reactive metals catalyze oxidation and hydroperoxide decomposition and thus increase the oxidation rate and both the hydroperoxide production and removal rate, while reactive sulfur species remove hydroperoxides and thus lower the hydroperoxide level and increase the removal rate. Also, polar phenols react with peroxy radicals and slow the oxidation rate, thus slowing the rate of production of hydroperoxides. Figure 4 also shows the hydroperoxide concentrations simulated by the kinetic mechanism. Although the hydroperoxide simulations are not as accurate as the dissolved oxygen simulations, the model predictions of hydroperoxide peak location and absolute peak concentration agree reasonably well with the measurements. This work is the first successful modeling of hydroperoxide concentration vs time over a range of jet fuel samples and does so concurrently with the modeling of dissolved oxygen consumption.

The ability to simulate oxidation rates and hydroperoxide profiles using a kinetic mechanism and measured species class concentrations over a range of fuel samples provides confidence that the mechanism correctly includes the most important reaction chemistry and that measured species class concentrations can be used to determine autoxidation reactivity of fuels.

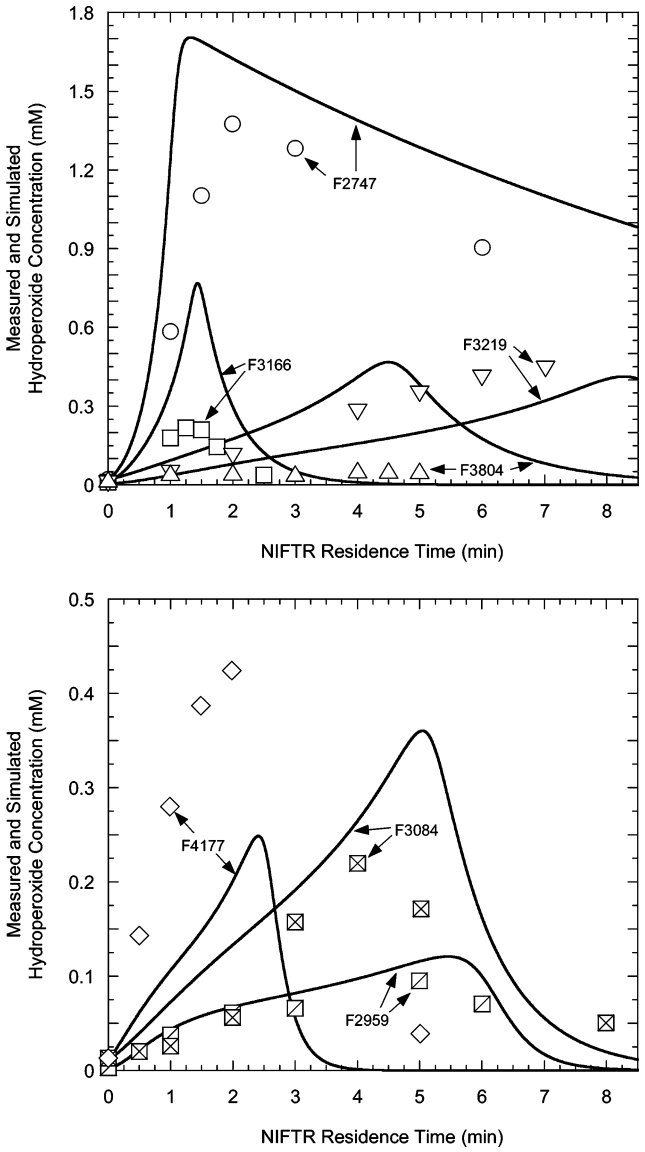

Figure 4. Comparison of measured and simulated hydroperoxide concentrations for seven fuels in the NIFTR at 185 °C. Symbols denote measurements. Curves denote chemical kinetic simulations: (a) F2747, F3166, F3219, and F3804; (b) F2959, F3084, and F4177.

These results also give confidence in beginning the next step, which is the development of a submechanism for production of surface deposits, toward the goal of enabling the prediction of jet fuel oxidation and deposition over a range of fuels, temperatures, and flow environments.

Computational Fluid Dynamics (CFD) Simulations of Jet Fuel Deposition. Despite numerous studies of the production of surface deposits during fuel autoxidation, very little is known about the chemical mechanisms which initiate and propagate this process. Here, it is hypothesized that deposits result, at least in part, from subsequent reactions of the autoxidation products of peroxy radical inhibitors (AH), such as naturally occurring phenols, and hydroperoxide decomposers (SH), such as fuel sulfides and disulfides. Such processes would account for the tendency of slow oxidizing fuels to form relatively high levels of deposits and fast oxidizing fuels to generate only low amounts of deposits,[24] as the same species which slow oxidation also increase deposition. In addition, it is likely that some subclass, or subclasses, of fuel nitrogen compounds (e.g., indoles and/or carbazoles) also contributes to surface deposition,[2,46] but the role of nitrogen species has not been explored in the present

(43) Striebich, R. C.; Grinstead, B.; Zabarnick, S. *J. Chromatogr. Sci.* **2000**, *38*, 393−398.
(44) Taylor, D. B.; Synovec, R. E. *Talanta* **1993**, *40*, 495−501.
(45) Taylor, D. B.; Synovec, R. E. *J. Chromatogr.* **1994**, *659*, 133−141.

Table 6. Candidate Global Deposition Submechanisms

deposit submechanism	reaction number	reaction type	reaction
a	19	wall	$Products_{AH} \rightarrow$ deposits
b	19	wall	$Products_{AH} + O_2 \rightarrow$ deposits
c	19	bulk	$Products_{AH} \rightarrow$ solubles
	20	bulk	$Products_{AH} \rightarrow$ insolubles
	21	wall	insolubles $\rightarrow$ deposits

work. In this section, the reactions which play a role in initiating surface deposition and the kinetics involved in these reactions are further explored. As the deposition process is poorly understood and extremely complex, the reactions employed here for the deposit submechanism are necessarily global in nature. That is, the reactions employed simulate a large amount of poorly understood chemistry and do not represent individual elementary reactions. Thus, Arrhenius parameters used in the deposition submechanism have no chemical significance, in contrast to the reactions of the oxidation mechanism (Table 2).

Various global reactions are available as candidates for the deposit submechanism. It is important to select a reaction or series of reactions that is able to reproduce the observed deposition profiles as well as the time, temperature, and flow dependencies of deposition. Reaction selection is also complicated by the fact that deposit formation reactions can occur directly at the wall surface, or initially in the bulk fuel with subsequent reaction or adherence on the wall. In selecting candidate global deposition reactions, the goal is to select the simplest reaction set which yields the observed deposition profiles over a range of fuels and reaction conditions. It is important to note that the deposition submechanism is closely coupled to the autoxidation mechanism discussed above. As deposition is directly related to the oxidation process, it is essential to correctly simulate the rates and oxidation profiles of a range of fuels to have an opportunity to model deposition properly. One limitation of the current autoxidation mechanism is that, while the hydrocarbon/oxygen part of the mechanism was developed over a range of temperatures,[6] the reactions of the species classes AH, SH, and metals have only been validated at a single temperature. This limitation needs to be considered in the non-isothermal deposition study reported below.

Three global deposition submechanisms were examined in this work, and they are listed in Table 6. Initial computational modeling indicated that, for the AH and SH species levels found in the current fuels and the conditions of the experiments reported here, deposit production due to SH reaction products was negligible relative to those produced via AH reaction products. Thus, for the current study, SH reaction products were not included in the deposition submechanism, although SH reaction products may need to be included in the future for deposition submechanisms employed for a larger set of fuels and/or other reaction conditions.

The first global deposition submechanism (submechanism a in Table 6) consists of a single, direct reaction of $Products_{AH}$ (i.e., the termination products of the reaction of $RO_2^{\bullet}$ with $A^{\bullet}$) at the wall to form deposits. This is the simplest and most direct path to deposits using the assumption that deposits result from AH oxidation reaction products. The second global deposition submechanism considered (submechanism b in Table 6) is also a single reaction where $Products_{AH}$ species react with dissolved oxygen at the wall to form deposits. The third global deposition submechanism (submechanism c in Table 6) consists of three reactions, where AH reaction products form both soluble and insoluble species in the bulk fuel, with subsequent reaction of the insoluble species at the wall to form deposits. The first two submechanisms are adaptations of initial reactions studied recently,[10] where oxygen was added in the second submechanism to provide improved deposition profiles. The third submechanism was created in the current study to provide improved agreement for the absolute deposit magnitude between the model calculations and the experiment measurements. These results are detailed below in studies of the modeling of deposition in near-isothermal (NIFTR) and non-isothermal (ECAT) reactors.

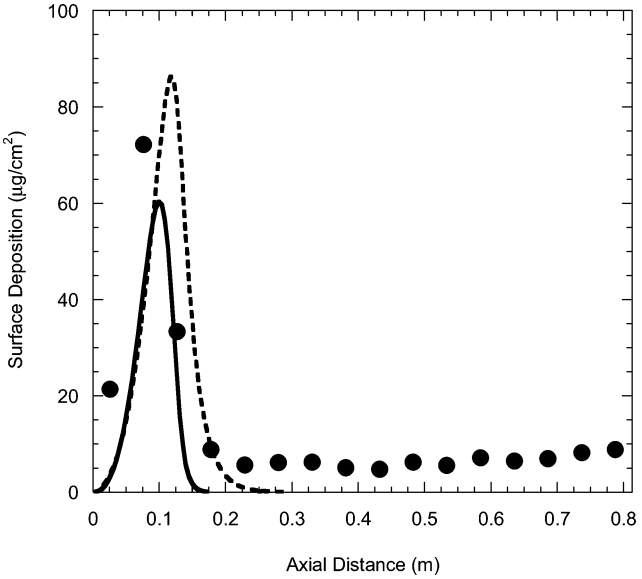

Figure 5. Comparison of measured and simulated deposit profiles for near-isothermal testing of jet fuel F2747. Symbols denote measurements, and curves denote computational fluid dynamics simulations for submechanism b (solid curve) and submechanism c (dashed curve).

Near-Isothermal Deposition. NIFTR deposition experiments on each of the seven fuels were performed at identical conditions of flowrate (0.25 mL min^{-1}), temperature (185 °C), and stress time (72 h). Thus, differences in deposition profiles and magnitudes among the fuel samples are driven by the varying chemical composition of the fuels and the resulting changes in oxidation rate and deposit forming tendencies. Figures 5−11 show the measured deposition of the seven jet fuel samples from these experiments. The figures show that the measured peak deposition varies by over an order of magnitude, ranging from ~10 (for fuel F3219) to ~160 μg cm^{-2} (for fuel F3166). The axial locations in the tube at which the peak deposition occurs also vary significantly from ~0.08 (F2747) to ~0.48 m (F2959 and F3219) and appear to be related to the oxidation rate. That is, fuels that oxidize quickly tend to exhibit peak deposition further upstream than those that oxidize more slowly. In addition, slow oxidizing fuels tend to have broader deposition peaks than fast oxidizing fuels.

In previous work under similar near-isothermal conditions, it has been noted that the axial location of the fuel autoxidative peak deposition is usually observed near the location of maximum oxidation rate.[47] Thus, if a proper deposition submechanism is employed, the CFD simulations should provide a good estimation of the location of the peak deposition over the range of fuels, as the autoxidation mechanism utilized here closely simulates the measured oxidation profiles. For a given global deposition submechanism, it is important to note that the only model inputs that are varied are the initial concentra-

(46) Taylor, S. E. *Prepr. Pap.—Am. Chem. Soc., Div Pet. Chem.* **2002**, *47*, 165−169.

(47) Jones, E. G.; Balster, W. J.; Post, M. E. 1993, ASME 93-GT-334.

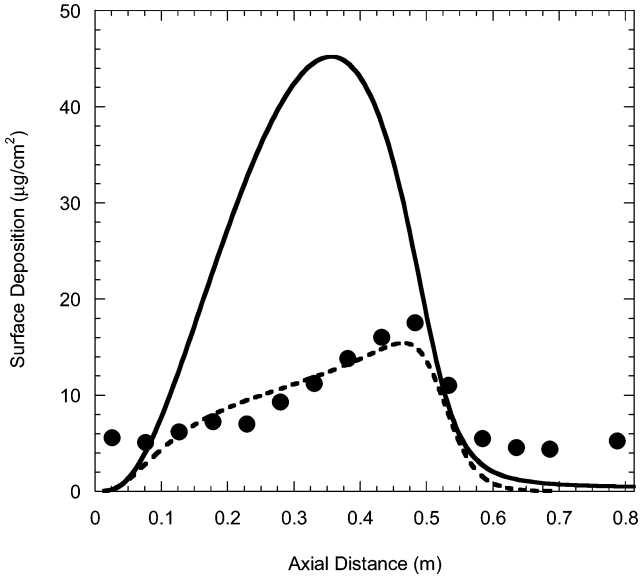

Figure 6. Comparison of measured and simulated deposit profiles for near-isothermal testing of jet fuel F2959. Symbols denote measurements, and curves denote computational fluid dynamics simulations for submechanism b (solid curve) and submechanism c (dashed curve).

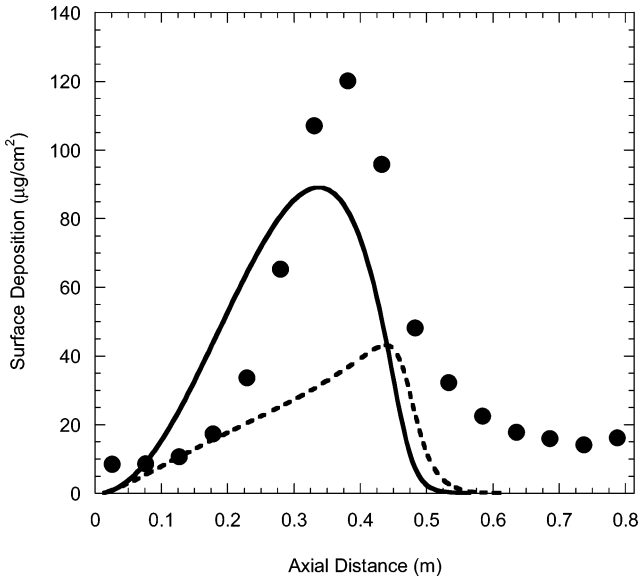

Figure 7. Comparison of measured and simulated deposit profiles for near-isothermal testing of jet fuel F3084. Symbols denote measurements, and curves denote computational fluid dynamics simulations for submechanism b (solid curve) and submechanism c (dashed curve).

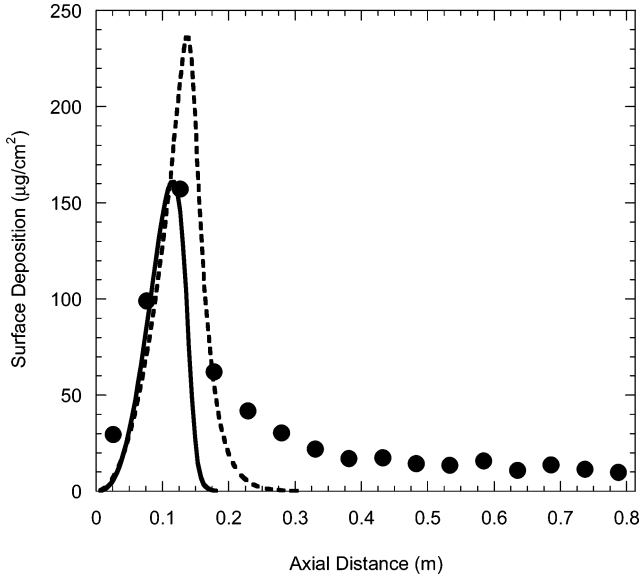

Figure 8. Comparison of measured and simulated deposit profiles for near-isothermal testing of jet fuel F3166. Symbols denote measurements, and curves denote computational fluid dynamics simulations for submechanism b (solid curve) and submechanism c (dashed curve).

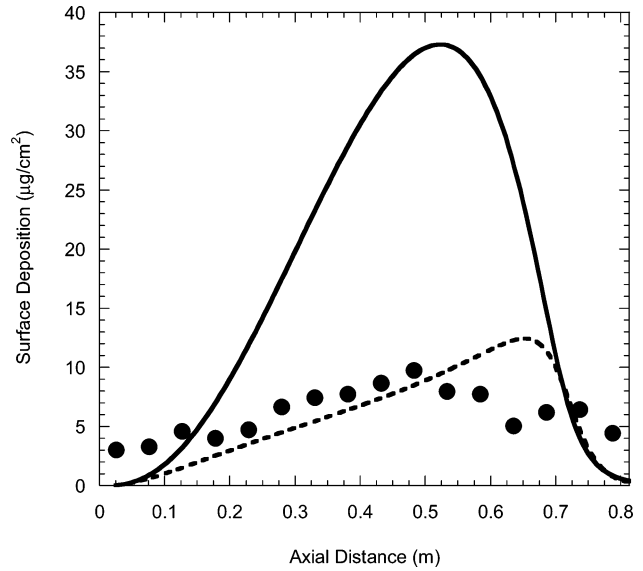

Figure 9. Comparison of measured and simulated deposit profiles for near-isothermal testing of jet fuel F3219. Symbols denote measurements, and curves denote computational fluid dynamics simulations for submechanism b (solid curve) and submechanism c (dashed curve).

tions of species classes (AH, SH, ROOH, and dissolved metals) for the various fuel samples. Reactions comprising the global deposit submechanisms are appended to the oxidation kinetic mechanism of Table 2. The rate constants at 185 °C of the global reactions in the deposit submechanism are calibrated by iterative adjustment of these values to provide the best match of deposit magnitude and axial location to the measured deposition profiles over the range of fuel samples. No constraints are placed on the values of the rate constants in the deposition submechanism as the reactions are global and are not meant to represent elementary chemical reactions.

The first global mechanism considered (submechanism a) is a single, direct reaction of AH reaction products at the wall to form deposits. This submechanism was found to yield reasonable simulations (not shown here) of the peak deposit locations for the NIFTR deposition experiments but was unable to simulate the magnitude of the deposition correctly. For relatively high values of the 185 °C rate constant for the deposition reaction, where all $Products_{AH}$ species result in the formation of deposits, the simulated peak deposit magnitude was orders of magnitude greater than the measurements. Reduction of the 185 °C rate constant resulted in a reduced magnitude of the simulated peak deposition, due to the resultant slowing of the reaction, but also yielded unacceptably large simulated deposits downstream of the peak. Thus, this simple deposit submechanism does not provide the correct reactions to allow proper simulation of the measured deposition and was not considered further.

Submechanism b was created to address the deficiencies in submechanism a, by adding oxygen as a reactant to the wall reaction of $Products_{AH}$. This modification should result in reduced deposition downstream of the oxygen consumption curve, as the deposition reaction rate is now proportional to the oxygen concentration. The results of using submechanism b are

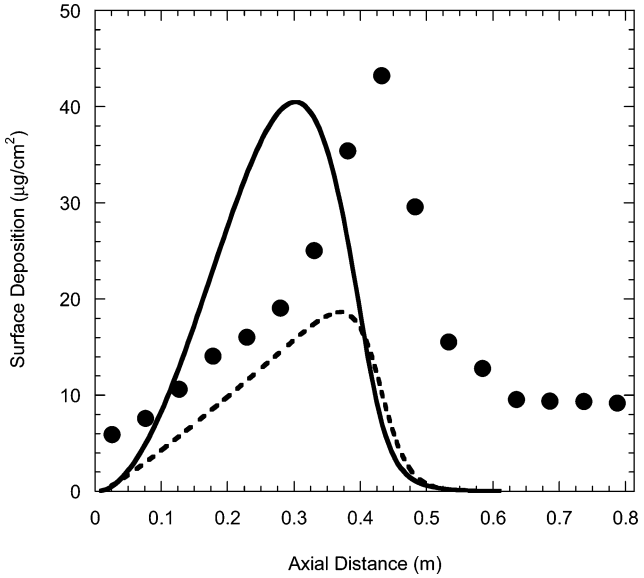

Figure 10. Comparison of measured and simulated deposit profiles for near-isothermal testing of jet fuel F3804. Symbols denote measurements, and curves denote computational fluid dynamics simulations for submechanism b (solid curve) and submechanism c (dashed curve).

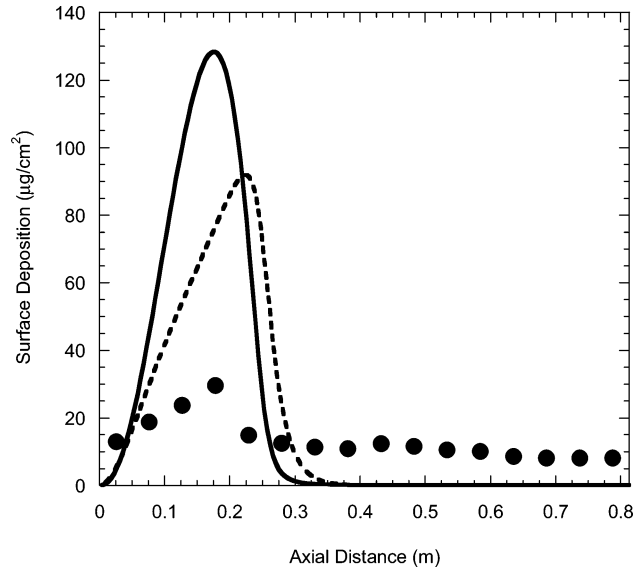

Figure 11. Comparison of measured and simulated deposit profiles for near-isothermal testing of jet fuel F4177. Symbols denote measurements, and curves denote computational fluid dynamics simulations for submechanism b (solid curve) and submechanism c (dashed curve).

compared with the experimental measurements in Figures 5−11 for each of the fuels. A 185 °C rate constant value of $k_{19b} = 5 \times 10^{-4}$ L mol^{-1} s^{-1} m^{-1} was found to most closely simulate the measured deposits. The plots show that the submechanism does a very good job of simulating the deposit peak location for all the fuels but does a better job of simulating the deposition magnitude for higher peak deposit fuels (e.g., F2747, F3084, and F3166) than for lower depositing fuels. For these higher peak deposit fuels, the simulation is within 30% of the measurement, but for the lower depositing fuels, the simulation is only within a factor of 4 and always greater than the measurement.

Submechanism c was created to address the deficiencies in submechanism b. This submechanism consists of a three-step scheme with two bulk reactions and a single wall reaction. In the two bulk reactions, Products_{AH} can react to form either soluble or insoluble precursors, and in the wall reaction, the insoluble precursors can react to form deposits. This submechanism creates a competition in which only a fraction of the products may react at the wall and provides the ability to more readily calibrate the model for deposition magnitude. With this submechanism, the location of the deposit peak is primarily a function of the oxidation rate and the rate of the wall reaction, while the deposit magnitude is primarily a function of the competition between the bulk reactions. It also provides for the formation of soluble and insoluble products, as well as wall deposits, all of which are known to form in fuel autoxidative systems. The plots in Figures 5−11 show that this submechanism also does a very good job at simulation of the axial location of the deposition peak for each of the fuels, but it also provides improved agreement with the measurements for the low peak depositing fuels. Rate constant values (185 °C) of $k_{19c} = 1 \times 10^{9}$ s^{-1}, $k_{20c} = 3 \times 10^{7}$ s^{-1}, and $k_{21c} = 5 \times 10^{-5}$ s^{-1} m^{-1} are used in the simulations and were again selected based on iterative analysis over the entire range of fuel samples. For the two lowest depositing fuels, F2959 and F3219, the submechanism provided very good agreement for the deposit magnitudes (within 30%) and profiles. For the other five fuels, the simulations yield deposit peak magnitudes that are from 20% to a factor of 3 of the measurements, without a propensity for being too high or low.

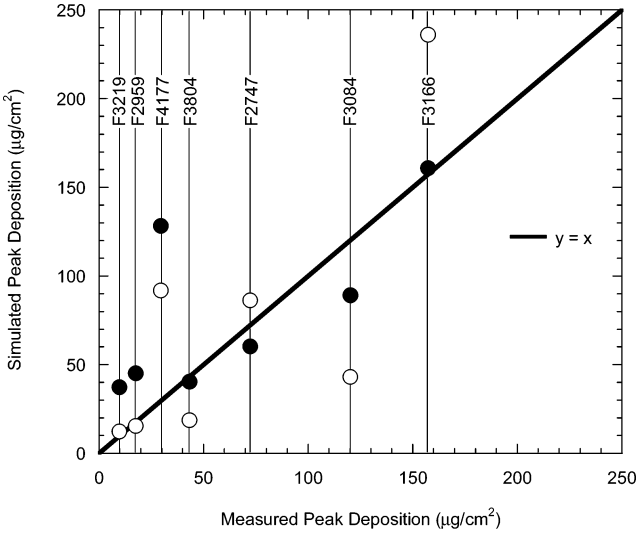

Figure 12. Comparison of measured and simulated peak deposition for seven jet fuel samples using global deposition submechanisms b and c of Table 6. Closed circles correspond to submechanism b, and open circles correspond to submechanism c.

Figure 12 provides a comparison of the measured and simulated peak deposition magnitude over the range of fuel samples using global deposit submechanisms b and c. For the lowest depositing fuels (F2959, F3219, and F4177), the three-reaction submechanism is more accurate than the single-reaction mechanism. For all remaining, higher depositing fuels, the single-reaction model is as accurate (F2747) or more accurate (F3804, F3084, and F3166) than the three-reaction mechanism. The results appear to indicate a change in the global deposit submechanism with increasing fuel deposit level. This may be due to a change of deposition chemistry which occurs as the tube surface develops an increasingly thick layer of deposit, perhaps because of entrapment of fuel in the deposit structure. Further elucidation of this effect will require additional studies with a significantly larger set of fuels. Both submechanisms are able to quantitatively simulate the deposit production magnitude and location within a factor of 4 for the fuel with the worst agreement and, more typically, within a factor of 2

Table 7. Rate Parameters for Three-Reaction Global Deposition Submechanism

reaction number	reaction	A	E_a (kcal mol^{-1})	k_{185C}
19	$Products_{AH} \rightarrow$ solubles	1×10^9 s^{-1}	0	1×10^9 s^{-1}
20	$Products_{AH} \rightarrow$ insolubles	3.8×10^{10} s^{-1}	6.5	3×10^7 s^{-1}
21	insolubles $\rightarrow$ deposits	3×10^3 s^{-1} m^{-1}	16.3	5×10^{-5} s^{-1} m^{-1}

for these conditions and range of fuels. Overall, the results show the ability to quantitatively simulate the deposit production magnitude and location in flow systems for various fuels using only readily measured species class concentrations. Further evaluation of the usefulness of the approach is performed in the next section via simulations of deposition occurring in a non-isothermal flowing environment.

Non-Isothermal Deposition. The near-isothermal deposition experiments and modeling reported above show the promise of utilizing the methodology described here for prediction of jet fuel deposition. The single-temperature, near-isothermal environment provides a simplified temperature condition which enabled development of the autoxidative and deposition mechanisms, as well as inclusion of measured species class concentrations. As fuel is subjected to severe temperature changes in aircraft fuel systems, it is essential to perform experimental and modeling simulations of such non-isothermal flow environments. The ECAT test rig is utilized here to evaluate the assumed oxidation and deposition mechanism and species class methodology on a flow environment in which the fuel undergoes substantial temperature increases throughout the test tube. Here, fuel F4177, a JP-8 fuel that is included in the set of seven fuels, is run in the ECAT at three temperature conditions (maximum wall temperatures of 340, 370, and 400 °C) with subsequent determination of the surface deposit axial profiles. As each of the ECAT experiments was performed with the same tubing, flow rate, and fuel, the differences in observed deposition behavior are controlled by differences in the thermal environment (e.g., the temperature-dependent chemistry). The oxidation mechanism and input species class concentration profiles are the same as those employed in the previous section. The three-reaction global deposition submechanism (submechanism c) is employed as it provided the best agreement for the near-isothermal deposition of this fuel. It is important to note that the 185 °C rate constant values determined for the global deposition reactions in analysis of the near-isothermal deposition are maintained here. However, in contrast to the near-isothermal simulations, the Arrhenius parameters of the deposit submechanism reactions need to be determined for these non-isothermal conditions. The approach taken here was to first "calibrate" the rate parameters (A and E_a) of the three global reactions for the mid-temperature experiment, subject to the constraint of matching the 185 °C rate constant values. The resulting mechanism is then utilized without any further modifications in simulations of the two additional non-isothermal experiments (one at a higher wall temperature and one a lower wall temperature). Thus, the accuracy of the simulated deposition for the higher and lower temperature experiments provides an indication of the predictive capability of the model with changes in temperature.

The calibration of the rate parameters for the global deposition reactions involved iterative comparisons of deposition simulations and measurements for the mid-temperature experiment. The rate parameters determined for these global reactions are shown in Table 7. The AH, SH, metals, and global deposit submechanism parts of the model have not previously been validated at varying temperature conditions, so these non-isothermal experiments, with temperatures from 21 to ~400 °C, provide a stringent evaluation of both the oxidation mechanism and deposition submechanism.

Figure 13 shows measurements of deposition for the three F4177 ECAT experiments. The figure shows that the peak deposition locations (~0.6−0.8 m) and magnitudes (~90−160 μg cm^{-2}) are temperature-dependent, where increasing the temperature results in a larger deposition peak which occurs earlier in the tube. The resulting deposit simulations are shown as curves in the figure and indicate that the axial locations of the simulated peak deposition agree quite well with the measurements for the three experiments. Although the rate parameters of the global reactions were constrained to match the 185 °C rate constant values established in the NIFTR deposition analysis, it was found that quite reasonable simulations of the magnitude and distribution of deposition were still obtained. It should be noted that while many sets of rate parameters for the global reactions can fit this constraint, the parameters employed here were found to provide the best fit to the data. These results indicate that the oxidation mechanism is useful over a broader and higher range of temperatures than has been previously validated.

For the mid-temperature case, which was used to calibrate the global reaction rate parameters, Figure 13 shows that the simulated peak deposition is within 5% of the measurement. In the transition from the mid-temperature case to the low-temperature case, the model correctly predicts a reduction in peak deposition magnitude along with a downstream shift in peak deposit location. In contrast, for the transition from the midtemperature case to the high-temperature case, the model does not predict an increase in peak deposit as is seen in the experimental measurements, although the simulated peak deposit

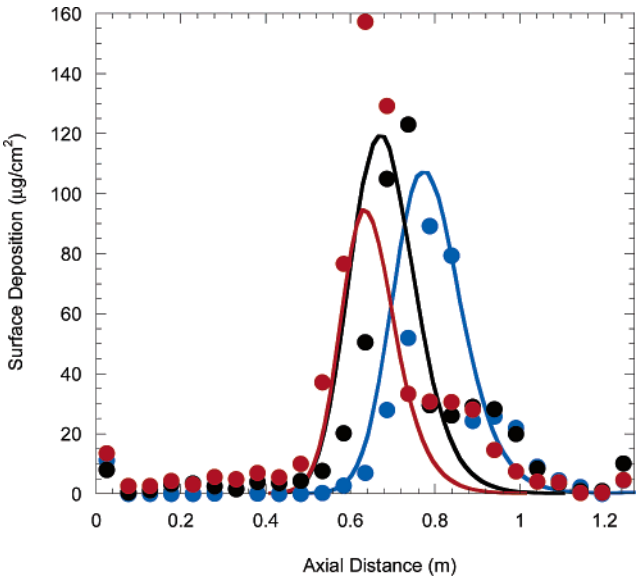

Figure 13. Comparison of measured and simulated deposition occurring in non-isothermal flowing environments for jet fuel sample F4177. Symbols denote measurements, and curves denote computational fluid dynamics simulations. The blue symbols/curve indicate the lowest-temperature experiment (340 °C maximum wall temperature), the black symbols/curve indicate the mid-temperature experiment (370 °C maximum wall temperature), and the red symbols/curve indicate the highest-temperature experiment (400 °C maximum wall temperature).

of the high-temperature case is within 60% of the measurement. Further analysis of species profiles for the high-temperature case indicates that the reduction in peak deposition in the simulation is due to reaction 16, $RO_2^{\bullet} \rightarrow R^{\bullet} + O_2$, of the mechanism becoming increasingly fast with temperature. Ultimately, this results in a slowing of the oxidation process and a corresponding reduction in deposition. Future work needs to examine in more detail the effect of this reaction, and the entire mechanism, on the temperature dependence of deposition.

The measured deposition profiles shown in Figure 13 each exhibit a shoulder on the downstream side of the deposition peak that is not predicted by the simulations. Additional work was performed (not shown here) to ascertain the source of this downstream shoulder. In these runs, ECAT deposits were measured at various test times. The results indicate that the shoulder becomes more prominent at shorter test times than the studies reported here. These results indicate that the shoulder is likely due to deposition which occurs during fuel/tube temperature stabilization during the startup of the test. During oven heatup, as the fuel approaches the ultimate test temperature, the fuel will be at various temperatures below the final temperature. At these lower temperatures, deposition will occur further downstream in the tube than at the final test temperature, thus generating an apparent shoulder in the deposition. Thus, the CFD model, which simulates the steady portion of the test run where the temperature at any point in the tube is constant, would not be expected to simulate this shoulder, which can be considered to be an artifact of the startup procedure of the experimental test.

Overall, the model does a very good job of simulating the deposit location and peak magnitude for this fuel over the wide range of temperatures to which the fuel is exposed during its transit through the tube. These results indicate that combining a suitable chemical kinetic mechanism with CFD modeling provides promise in simulating oxidation and deposition in the complex temperature and flow environment encountered in actual aircraft fuel system components.

Future Work. While the results reported here indicate that the methodology of using species class measurements along with a chemical kinetic mechanism for the simulation of oxidation and deposition is quite feasible, the method needs to be further refined in a number of important areas. These include improved species class analyses, improved understanding of the role of species classes and their interactions, refinements in the chemical kinetic mechanism, additional deposition and oxidation experimental data over wider ranges of conditions, and additional experimental data on a larger set of fuel samples. In particular, the role of metal and nitrogen species in the autoxidation process needs to be better understood so that these species can be properly included in the mechanism. In addition, improved analysis methods are needed for both the metal and nitrogen species classes. The metal species need to be measured accurately in the parts per billion range and speciated into reactive and nonreactive components, while methods need to be developed to quantify the nitrogen species by species class (e.g., indoles, carbazoles, etc.). In addition, more work needs to be performed to determine the concentrations and temperatures at which various fuel metals species begin to play a role in catalysis. The mechanism needs to be modified to include the differences in reactivity between hindered and nonhindered phenols, as hindered phenols are more efficient at intercepting peroxy radicals but are likely less efficient at producing deposition. Analysis techniques need to be developed to differentiate between these species as classes. Also, the mechanism needs to be modified to include the different roles of paraffinic and aromatic species, as it currently does not differentiate between these species which have very different reactivities in these systems. Additional experimental data needs to be acquired over a wide range of temperatures to better simulate the range of temperatures to which fuel is exposed in aircraft fuel systems. This additional data will help better determine the proper Arrhenius parameters that are required in the mechanism. Data over a wide range of temperature may also indicate other reactions that may need to be included under extrapolated conditions, e.g., relatively high and low temperatures. The increasingly important role of peroxy radical decomposition at higher temperatures is an example of the type of information which resulted from the present study. In addition, further studies of fuel autoxidation are needed to better understand the complexities of acid/base catalysis on autoxidation, the role of metal surfaces on the catalysis of deposition, and the role of metal deactivators on bulk and surface deposition. Improvements in all of the reactions of the mechanism will come with future studies on techniques to determine the Arrhenius parameters of the reactions of interest.

Ultimately, the fuel system and fuel component designer are concerned with the deposition which occurs over the lifetime of the component, which is exposed to many fuels over thousands of hours. Thus, future work also needs to address the expected average deposition produced over a typical variety of fuel samples, so that designers can use simulations such as these to modify their component designs and/or limit temperatures to minimize deposition in critical areas. In addition, studies of flow and deposition in complex geometries which simulate the aircraft engine nozzle environment are necessary.

Conclusions

This paper describes the development of a modeling methodology to enable the prediction of liquid-phase autoxidation and deposition of jet fuels. A chemical kinetic mechanism developed previously is refined to include the roles of key fuel species classes, such as phenols, reactive sulfur species, dissolved metals, and hydroperoxides. The concentrations of these fuel species classes in the unreacted fuel samples are measured experimentally and used as an input to the mechanism. The resulting model is used to simulate the autoxidation behavior observed over a range of seven fuel samples. The model includes simulation of the consumption of dissolved oxygen, as well as the formation and consumption of hydroperoxide species during thermal exposure. Proportional relationships were developed to incorporate the measured species class concentrations into the chemical kinetic mechanism. The fuel catalytic metal species are modeled using the Cu and Mn species measured in the fuels. The presence of metal deactivating additive is shown to result in a lower required level of metals in the model input than the experimental measurements for two of the seven fuels. Oxygen consumption and hydroperoxide profiles are obtained in a near-isothermal flow system at a temperature of 185 °C. The model is able to satisfactorily simulate these oxidation and hydroperoxide profiles for each of the seven fuels, using a constant chemical kinetic mechanism and by only varying the species class concentrations to differentiate the fuels.

Computational fluid dynamics simulations of isothermal and non-isothermal deposition experiments were performed to evaluate candidate global deposition submechanisms. Three global deposition submechanisms were evaluated, and two were found to yield reasonable simulations of deposit peak location and magnitude. These deposit submechanisms involve the

reaction products of polar phenol species in the formation of deposits. Including reactive sulfur species in the global deposition mechanisms did not improve agreement with the experiment, and as such, these species were not employed in the deposit submechanisms. CFD simulations were also performed for one fuel sample stressed in a non-isothermal flowing system at three different tube wall temperatures. The model simulations closely matched the location of the deposition peaks but were less satisfactory at simulating the increasing deposit peak magnitude with temperature due to limitations of the oxidation mechanism at high temperatures. Future work to improve the methodology was presented and included improved species class analyses, improved understanding of the role of species classes and their interactions, refinements in the chemical kinetic mechanism, additional deposition and oxidation experimental data over wider ranges of conditions, and additional experimental data on a larger set of fuel samples.

Acknowledgment. This work was supported by the Air Force Research Laboratory, Propulsion Directorate, Turbine Engine Division, Fuels Branch, Wright-Patterson AFB, OH, under Contract No. F33615-03-2-2347. This work was also supported in part by the Air Force Office of Scientific Research (AFOSR). Julian Tishkoff is the AFOSR Program Manager. The U.S. Government is authorized to reproduce and distribute reprints for Governmental purposes notwithstanding any copyright notation thereon. The views and conclusions contained herein are those of the authors and should not be interpreted as necessarily representing the official policies or endorsements, either expressed or implied, of the Air Force Research Laboratory or the U.S. Government. The authors would also like to acknowledge Lori Balster of UDRI for the polars analysis, Donald Minus of AFRL for the reactive sulfurs analysis, Tony Viscomi of the Air Force Petroleum Office (WR-ALC Det 3) for the dissolved metals analysis, and Matthew DeWitt and Dave Brooks of UDRI for the ECAT deposition experiments.

Note Added after ASAP Publication. In the version of this paper published on February 1, 2007, there were some errors in Table 5. These have been corrected in the version published on February 7, 2007.

EF060391O